Polymerized 4-Fold Coordinated Carbonate Melts in the Deep Mantle

Chrystèle Sanloup, Jessica Hudspeth, Veronika Afonina, Benjamin Cochain, Zuzana Konôpková, Gerald Lelong, Laurent Cormier, Chiara Cavallari

frontiers

Polymerized 4-fold coordinated carbonate melts in the deep mantle

Chrystèle Sanloup [1,*], **Jessica M. Hudspeth** [2], **Veronika Afonina** [3], **Benjamin Cochain** [2], **Zuzana Konôpková** [4], **Gérald Lelong** [1], **Laurent Cormier** [1] and **Chiara Cavallari** [5]

[1] *Institut de Minéralogie, Physique des matériaux et Cosmochimie, Sorbonne Université, CNRS, 75005 Paris, France*
[2] *Institut des Sciences de la Terre de Paris, Sorbonne Université, CNRS, 75005 Paris, France*
[3] *SUPA, Centre for Science at Extreme Conditions and School of Physics and Astronomy, University of Edinburgh, EH9 3FD, UK*
[4] *DESY Photon Science, Notkestr. 85, 22607 Hamburg, Germany*
[5] *European Synchrotron Radiation Facility, ESRF, 71 Avenue des Martyrs, 38000 Grenoble, France*

Correspondence*:
Corresponding Author
chrystele.sanloup@sorbonne-universite.fr

ABSTRACT

Our understanding of the deep carbon cycle has witnessed amazing advances in the last decade, including the discovery of tetrahedrally coordinated high pressure (P) carbonate phases. However, little is known about the physical properties of their molten counterpart at moderate depths, while their properties at lower mantle conditions remain unexplored. Here, we report the structure and density of $FeCO_3$ melts and glasses from 44 GPa to 110 GPa by means of *in situ* x-ray synchrotron diffraction, and *ex situ* Raman and x-ray Raman spectroscopies. Carbon is fully transformed to 4-fold coordination, a bond change recoverable at ambient P. While low P melts react with silica, resulting in the formation of silico-carbonate glasses, high P melts are not contaminated but still quench as glasses. Carbonate melts are therefore polymerized, highly viscous and poorly reacting with silicates in the lower mantle, in stark opposition with their low P properties.

Keywords: carbonate melts, high pressure, x-ray diffraction, Raman, X-ray Raman, polymerization, deep mantle

1 INTRODUCTION

Although the lower mantle is mostly a reducing environment with the presence of reduced Fe (Frost et al., 2004; Smith et al., 2016), significant amount of subducted carbonates are estimated to be preserved (Litasov and Shatskiy, 2018). Transition to 4-fold carbon was first predicted for crystalline $CaCO_3$ (Oganov et al., 2006; Arapan et al., 2007). This transition strongly depends on the carbonate composition, occuring for $CaCO_3$ above 105 GPa (Lobanov et al., 2017), 80 GPa for $MgCO_3$ (Oganov et al., 2008; Boulard et al., 2011), and 50 GPa for $FeCO_3$ (Liu et al., 2015), while intermediate $CaCO_3$-$MgCO_3$-$FeCO_3$ compositions form a single tetrahedral carbonate phase (Merlini et al., 2017) unlike silicates. This transition induces

polymerization such as sheets or 3-membered rings for $MgCO_3$ (Oganov et al., 2008), and chains for $CaCO_3$ (Oganov et al., 2006). In contrast, our knowledge of carbonate melts structure at depth is scarce and limited to upper mantle pressures. The melting curves of $CaCO_3$, Na_2CO_3, and $FeCO_3$ have been measured over most of the upper mantle regime (Li et al., 2017; Kang et al., 2015), and viscosity measurements up to 6 GPa span several compositions ($K_2Ca(CO_3)_2$ and $K_2Mg(CO_3)_2$ by Dobson et al. 1996, $CaCO_3$ and natural dolomite by Kono et al. 2014, Na_2CO_3 by Stagno et al. 2018). Structural data instead have only been collected on molten $CaCO_3$ below 10 GPa (Hudspeth et al., 2018) while theoretical investigations of the properties of carbonate melts cover a larger P-range but are also limited to the carbon 3-fold stability field (Vuilleumier et al., 2014; Zhang and Liu , 2015; Du et al., 2018; Desmaele et al., 2019). One main question is therefore how this 3-fold to 4-fold transition translates in the molten state, and what are the consequences on the physical and chemical properties of carbonate melts? Of particular interest is the mobility and reactivity of carbonate melts in the lower mantle, knowing that these properties underpin the key role played by carbonate melts in mantle geodynamics through lubrication of plate tectonics, cratonic roots (Foley, 2008) and ascending plumes (Litasov et al., 2013).

The role of Fe in the deep carbon cycle is emphasized by the predominance of Fe-rich ferropericlase in diamond inclusions from the lower mantle (Kaminsky, 2012). The lowest transition P from 3-fold to 4-fold C in $FeCO_3$ amongst carbonates justifies its choice as the first composition to investigate. Not only this transition occurs at less challenging experimental conditions, but it might be driven by Fe high spin to low spin transition at 40.4 GPa (Weis et al., 2017), a consequence of which being the large enrichment in Fe of (Mg,Fe)-carbonates coexisting with bridgmanite to almost pure $FeCO_3$ (Lobanov et al., 2015). Besides, high Fe concentration stabilizes $(Ca,Mg,Fe)^{IV}CO_3$ with respect to single cation 3-fold carbonates at mid mantle conditions (30-50 GPa) (Solomatova and Asimow, 2018). Formation of Fe-carbonates in the lower mantle might also result from carbonation of Fe-oxides ((Mg,Fe)O, FeOOH) with CO_2 (Boulard et al., 2012, 2018). Last but not least, $FeCO_3$ is a technical choice as it can be laser heated, which is required to reach lower mantle conditions without the need for additional laser coupler.

2 MATERIAL AND METHODS

Materials and chemical analyses

The starting natural crystalline siderite sample (mineralogical collection at Sorbonne Université) was loaded in the sample chamber laser-drilled in a rhenium gasket as approximately 20 µm-thick platelet between two equally thick platelets of compressed SiO_2 powder. The SiO_2 platelets act as thermal insulators and P-transmitting medium. Only one sample was used per P point (Fig.1) to avoid repeated laser-heatings, and preserve the chemical integrity of the sample. Six samples could be recovered after the experiments, embedded in epoxy and polished for analysis. Samples 8, 9 and 15 were carbon-coated for SEM imaging (Fig.2), samples 8 and 15 were then repolished and gold-coated along with samples 13, 14 and 20 for electron microprobe analysis using a CAMECA SX-FIVE analyzer (EMPA) at the Camparis centre of Sorbonne Université (Table 1), using the following operating conditions: 15 keV, 10 nA. We used a defocussed beam size of 10 µm to get an average composition at the laser-heated spot.

P-T conditions

We used diamond-anvil cells and a double-sided infra-red laser focussed down to 20 µm to generate high T and P. For each P point, targeted power was increased in 2 W increments from 20 to 50 W of power on each laser depending on P until complete melting of the sample. Melting was identified by disappearance of diffraction peaks apart from SiO_2 peaks, and by the appearance of diffuse scattering. As we used the

off-axis heating system to avoid using carbon mirrors that would add to the x-ray background signal and compromise processing of the scattered signal, T could not be measured by pyrometric techniques. $FeCO_3$ melting curve has only been measured up to 20 GPa (Kang et al., 2015), where it reaches 1865 K. The stishovite to $CaCl_2$ SiO_2 transition has been investigated up to 90 GPa (Fischer et al., 2018), this constrains T to a maximum of 2300 K at 79 GPa and 2500 K at 83 GPa as $CaCl_2$ is the observed SiO_2 structure for the three highest P runs, while stishovite is observed below. We therefore consider that x-ray diffraction patterns were collected on molten $FeCO_3$ within the 2000 K- 2500 K interval except for the highest P point that is only constrained to below 3500 K from extrapolation of the stishovite-$CaCl_2$ Clapeyron slope (Fischer et al., 2018). P is measured at room T using fluorescence of a ruby sphere added in the sample chamber (Mao et al., 1986) and SiO_2 equations of state (Andrault et al., 1998; Nishihara et al., 2005) for quenched samples, and using only SiO_2 equations of state for molten samples with error bars on P including the effect of a 2000 K-2500 K T-range, and up to 3500 K for the 110 GPa data point.

X-ray diffraction methods

We collected *in situ* high P-T x-ray diffraction data in laser-heated diamond anvil cells at the extreme conditions beamline P02.2 at the PETRAIII synchrotron. We used symmetric diamond-anvil cells equipped with 70° opening Boehler-Almax seats in order to access a wider q-range up to 10 $Å^{-1}$, and reduce the diamond Compton contribution as Boehler-Almax anvils are only 1.5 mm thick. The x-ray monochromatic beam (42.7 keV) was focussed down to a size of 4 × 6 $μm^2$, allowing high spatial resolution in direct space. To limit iron migration away from the laser heating spot due to Soret effect, the laser shutters were opened only once the targeted power was reached, and held open for 10 s during which 10 x-ray diffraction patterns of 1 s acquisition time were recorded on a Perkin-Elmer 2-D detector. 2-D patterns were integrated using the Fit2D software (Hammersley et al., 1996). In order to isolate the scattered intensity from the molten $FeCO_3$ only, each sample was removed from the gasket, and the gasket put back in place to collect x-ray data on the empty cell. Obtained patterns were then scaled vertically to match the baseline of x-ray patterns collected on the starting crystalline sample under P (Sanloup and de Grouchy, 2018). This last step ensures that any P effect on the background is corrected for. Amongst eight successful runs (Table 1) for which full melting was observed, intensity from molten $FeCO_3$ could only be processed for the highest P run for which the sample *vs* SiO_2 platelets thickness ratio was slightly higher, the scattered intensity being too weak for the lower P points. All glass patterns could be processed. The x-ray diffracted intensity data are converted into the structure factor, $S(q)$ (Fig.**??** and Fig.4), using the Ashcroft-Langreth formalism. The radial distribution function $g(r)$ (Fig.3B), that describes ion-ion contributions in real space, is obtained by Fourier transforming of $S(q)$,

$$g(r) = \frac{1}{2\pi^2 rn} \int_0^\infty qS(q)\sin(qr)\,dq \tag{1}$$

where $n = \frac{\rho \mathcal{N}_A}{M}$, $\mathcal{N}_A$ is the Avogadro number, M the mean atomic molar mass, and ρ the density.

Density measurements

The method to derive density from x-ray diffraction data on melts compressed in diamond-anvil cell experiments (Eggert et al., 2002; Sanloup et al., 2013) consists in minimizing the oscillations in $g(r)$ where there should not be any signal, *i.e.* below the minimum interatomic distance ($r < 0.95$ Å here). This method requires that the background, essentially the Compton signal from the diamond anvils that dominates the total diffracted intensity, is perfectly subtracted.

As the C-O contribution is distinct on $g(r)$ of quenched glasses up to 83 GPa, we also ran consistency checks by fixing the C-O coordination number to 4 as indicated by x-ray Raman spectra (*cf* Results section), and simulating the C-O contribution using the obtained density values against a gaussian with the following equation:

$$g(r) = \frac{1}{nS_\infty}\frac{A}{\sigma\sqrt{2\pi}}exp\left(-\frac{(r-d)^2}{2\sigma^2}\right) \quad (2)$$

where

$$S_\infty = \frac{\Sigma_p K_p^2}{Z_{tot}^2} \quad (3)$$

and

$$A = \frac{CN}{\int \frac{4\pi r^2}{\sigma\sqrt{2\pi}}exp\left(\frac{-(r-d)^2}{2\sigma^2}\right)dr} \quad (4)$$

with K_p, the effective atomic number (Eggert et al., 2002), Z_{tot} the total atomic number of the compositional unit (*e.g.* $FeCO_3$), CN the C-O coordination number fixed to 4, d the C-O inter-atomic distance, and σ a parameter depending on structural disorder, $\sigma = k\sqrt{d}$ where k is an adjustable parameter (Hosemann and Bagchi, 1962) with a value of 0.11 here. The C-O contribution to $g(r)$ thus calculated adequately fits the experimental ion-ion contribution (dashed lines on Fig.3B), hence comforting the obtained density values.

X-ray Raman and Raman methods

Raman and x-ray Raman spectra were collected at ambient conditions on glassy $FeCO_3$ recovered from x-ray diffraction experiments and from additional laser-heated diamond anvil cell synthesis respectively. X-ray Raman data were collected at an incident energy of 9.7 keV at the C K-edge on beamline ID20 of the European Synchrotron Radiation Facility (ESRF), beamsize was 15×15 µm^2. The large-solid-angle x-ray scattering spectrometer (Huotari et al., 2017) was set up with 24 Si(660) analyzer crystals for an average momentum transfer of 7.3 ± 0.2 Å^{-1} and an overall energy resolution of 0.7 eV. All experimental data were analyzed using the XRStools software package (Sahle et al., 2015). The integrated intensity of each spectrum was normalized over a 35 eV energy range. Glassy $FeCO_3$ spheres had been previously synthesized at 59 GPa using the same P02.2 laser heating system in PetraIII as for x-ray diffraction experiments. LiF was used instead of SiO_2 as a P-transmitting medium to avoid any contamination of the x-ray Raman signal by oxygen from SiO_2 as measurements at the O K-edge were initially planned but signal was to weak for data to be processed. Despite its higher melting curve than siderite (Boehler et al., 1997), LiF salt could not be used for the x-ray diffraction experiments due to its continuous powder diffracted signal that prevents a qualitative analysis of the diffuse scattering signal from molten $FeCO_3$. Raman spectra were collected on glassy $FeCO_3$ recovered from x-ray diffraction experiments using 633 nm wavelength in order to preserve the samples, using more energetic lower wavelengths resulted in dissociation of the sample and detection of hematite signal.

3 RESULTS

All samples are systematically quenched as a glass. Chemical integrity of $FeCO_3$ molten spheres is observed for runs conducted above 40 GPa, apart from a marginal fraction at the glass-SiO_2 interface in one sample showing enrichment of the P-transmitting medium in Fe and C. Instead, the lowest P samples, *i.e.* 11 GPa and 15 GPa, have reacted with the SiO_2 P-transmitting medium. This is shown by SEM imaging (Fig.2) and EMPA analysis on sample 8 (Table 1). High P carbonate melts are thus much less reactive than low P

melts. This might not contradict the observed reactivity of high P crystalline $MgCO_3$ with SiO_2 (Seto et al., 2008; Maeda et al., 2017) due to the much longer heating durations (20-240 minutes against 10 seconds heating duration in this work); alternatively, Fe stabilizing effect on high P carbonates could be at stake. We observe no disproportionation of Fe as was reported in the crystalline state in some studies (Boulard et al., 2011; Cerantola et al., 2017) but not in others (Liu et al., 2015). This might be due to different P-T paths followed, *i.e.* flash heating here instead of continuous T increase (Boulard et al., 2011; Cerantola et al., 2017).

A striking characteristic of glassy $FeCO_3$ is its strong first sharp diffraction peak (FSDP) that persists in the structure factor up to the highest P investigated (Fig.3A), indicative of a strong medium-range order. This is in stark contrast to silicate glasses that lose their medium-range order with increased P (Sato and Funamori, 2008), but consistent with *ab initio* calculations on carbon-bearing silicate melts reporting P-induced polymerisation of carbonate species into dimers and with the silicate network (Ghosh et al., 2017; Solomatova and Asimow, 2019). A second noticeable feature is the decrease of the contribution at 4 $Å^{-1}$ attributed in molten carbonates to the O-O bond (Wilding et al., 2016). On radial distribution functions, $g(r)$ (Fig.3B), the C-O contribution is clearly visible at 1.2-1.3 Å with none or little overlap with the second contribution (Fe-O and O-O) at $\sim$2 Å in the glass, and with some overlap in the melt. No significant structural changes are observed between molten and quenched glassy state at 110 GPa, apart from a generally lower intensity in the melt due to the high T and consequent higher degree of disorder. For $g(r)$, this weaker intensity translates into broader C-O and Fe-O/O-O contributions in the molten state. For glasses quenched at 11 GPa and 15 GPa, the x-ray structure factor, $S(q)$, is intermediate between that of pure SiO_2 glass (Sato and Funamori, 2008) and high-P $FeCO_3$ glasses (Fig.4). SEM image of sample 8 (15 GPa, Fig.2) shows heterogeneities in the quenched glass, which indicates that the x-ray structure factor likely averages at least two types of glass structure and therefore data cannot be interpreted quantitatively.

The x-ray Raman C K-edge spectrum of quenched $FeCO_3$ glass shows no presence of sp2 3-fold carbon characterized by an intense π^* peak at 290 eV (Fig.5, π^* peak). Only the σ^* peak of tetrahedrally coordinated carbon (Shieh et al., 2013) is visible (Fig.5, σ^* peak). The totally missing π^* peak is indicative of a fully sp3 state of carbon atoms in the siderite glass. P-induced coordination changes of major cations in silicate melts (*e.g.* Si, Al) were first reported from the study of glasses quenched from high P (Meade, Hemley and Mao, 1992; Yarger et al. , 1995), and later confirmed by *in situ* studies in the molten phase (Sanloup et al., 2013; Drewitt, 2015). However, the opposite, *i.e.* coordination change occurring only in the quenched glass, not in the high P melt, have not been reported nor been theoretically predicted. The 3-fold to 4-fold transition therefore occurs in molten Fe-carbonates at P less or equal to 51 GPa. This transition is preserved upon quenching to the glassy state, and is recoverable at ambient conditions, opening the way to the synthesis of a new class of glassy materials. Two broad bands are observed in the Raman spectra (Fig.6), very different from those of the only two carbonate systems that quench as glasses at room P, $MgCO_3$-K_2CO_3 and $La(OH)_3$-$Ca(OH)_2$-$CaCO_3$-CaF_2BaSO_4 (Sharma and Simons, 1979), that are essential dominated by the strong CO_3^{2-} stretching mode at $\sim$1080 cm^{-1}. Instead, present Raman spectra are reminiscent of those reported for calcium silicate glasses (Fig.6) albeit at higher Raman shift values for the broadest band (1200-1600 cm^{-1} for glassy $FeCO_3$ *vs* 850-1100 cm^{-1} for calcium silicate glasses).

Density values are reported in Fig.7 along with predictions for lower P melt properties (Kang et al., 2015), P-evolution of crystalline siderite, and with the Earth's seismological PREM model (Dziewonski and Anderson, 1981). Density profile below 40 GPa is calculated using $K_{T,0}$ value of 80.23 GPa (Kang et al., 2015), consistent with that reported for molten calcite (Hudspeth et al., 2018), and density at room P of 2500 $kg{\cdot}m^{-3}$ by assuming a similar density jump upon melting as for other carbonates for which

room P density is known. Comparison with PREM model shows that Fe-carbonate melts are buoyant at all depths. Density contrast between the high P polymerized melt or glass and extrapolated equation of state for low P melt is approximately 15%, *i.e.* similar to volume collapse reported upon transition from crystalline high spin siderite I to low spin siderite II (Liu et al., 2015). The volume collapse is smoothed out over a $\sim$ 30 GPa range in the molten state with, as a direct consequence, a steepening of the melting curve from 55 GPa on (Cerantola et al., 2017).

4 DISCUSSION

The 3-fold to 4-fold transition occurs in molten Fe-carbonates at P less or equal to 53 GPa, compared to 50 GPa for crystalline $FeCO_3$ (Liu et al., 2015), 80 GPa for $MgCO_3$ (Oganov et al., 2008; Boulard et al., 2011), and 130 GPa for $CaCO_3$ (Oganov et al., 2006; Arapan et al., 2007). A consequence of the effect of Fe on the 3-fold C to 4-fold C transition P is that crystalline Fe-poor $(Ca,Mg,Fe)^{III}CO_3$ and Fe-enriched $(Ca,Mg,Fe)^{IV}CO_3$ melts could co-exist at depth. In the case of Si isotopes, fractionation between ^{VI}Si bridgmanite and ^{IV}Si olivine structures is theoretically estimated to ~ -1 ‰^{28}Si at 2000 K (Huang et al., 2014). If this effect can be scaled to C simply using mass difference considerations, then a few ‰^{13}C fractionation is expected, and could potentially explain isotopic differences between calcite inclusions from super-deep diamonds (Kaminsky et al., 2016). This effect might be sufficient to confer a mantle-like signature to deep diamonds grown from slab-derived carbonate melts while co-existing tetrahedral crystalline carbonate are expected to get lighter.

Density of non-crystalline $FeCO_3$ remains considerably lower than that of its crystalline counter parts, even at the highest investigated P, by approximately 15%. The situation is thus very different from that of molten and crystalline silicates which density converge at deep mantle conditions (Petitgirard et al., 2015; Sanloup, 2016), and such difference could be attributed to the very strong medium-range order preserved in tetrahedral high P carbonate melts while it is mostly collapsed by 5 GPa in silicate melts. That high P $FeCO_3$ melts quench as glasses contrasts with the behaviour observed at lower P, and suggests an important increase of carbonate melt viscosity consistent with the observation of a very strong medium-range order. It is also opposite to the behaviour of molten basalt that systematically quenches as crystalline phases above 11 GPa (Sanloup et al., 2013) and as a glass below. The strongly reduced chemical reactivity of high P $FeCO_3$ melts with silica along with their glass-forming ability suggest that unlike at lower P, tetrahedral carbonate melts are not pervasive, which could contribute to the longevity of carbonates in the deep mantle where allowed by oxydizing conditions or slow reduction kinetics (Litasov and Shatskiy, 2018).

CONFLICT OF INTEREST STATEMENT

The authors declare that the research was conducted in the absence of any commercial or financial relationships that could be construed as a potential conflict of interest.

AUTHOR CONTRIBUTIONS

J.H. and C.S. devised the project, C.S. processed x-ray diffraction data and wrote the paper with input from G.L. and L.C.. J.H., C.S., B.C., V.A., Z.K. participated in x-ray diffraction data acquisition. J.H., G.L., L.C., C.S. participated in x-ray Raman data acquisition. J.H. collected Raman data.

FUNDING

The research leading to these results has received funding from the European Community's Seventh Framework Programme (FP7/2007-2013) under grant agreements no. 312284 and 259649 (European Research Council starting grant to C.S.). Portions of this research were carried out at the light source PETRA III at DESY, a member of the Helmholtz Association (HGF). The laser heating system on beamline P02.2 is funded by the German BMBF (project number 05K10RFA).

ACKNOWLEDGMENTS

We acknowledge E. Boulard for providing the starting siderite sample, K. Glazyrin for his help with *ex situ* diamond-anvil cell laser-heating synthesis in PETRA III, L. Rémusat at Museum National d'Histoire Naturelle (Paris, France) for gold coating of the recovered samples, the ESRF (Grenoble, France) and PETRAIII (Hamburg, Germany) for provision of synchrotron radiation facilities.

REFERENCES

Andrault, D., Fiquet, G., Guyot, F., and Hanfland, M. (1998). Pressure-induced Landau-type transition in stishovite. *Science* 282, 720–724. doi:10.1126/science.282.5389.720.

Arapan, S., De Almeida, J. S., and Ahuja, R. (2007). Formation of sp(3) hybridized bonds and stability of $CaCO_3$ at very high pressure. *Phys. Rev. Lett.* 98, 268501. doi:10.1103/PhysRevLett.98.268501.

Boehler, R., Ross, M., and Boercker D. B. (1997). Melting of LiF and NaCl to 1 Mbar: Systematics of Ionic Solids at Extreme Conditions *Phys. Rev. Lett.* 78, 4589–4592.

Boulard, E., Gloter, A., Corgne, A., Antonangeli, D., Auzende, A.-L., Perrillat, J.-P., et al. (2011). New host for carbon in the deep Earth. *Proc. Natl Acad. Sci. USA* 108, 5184–5187. doi:10.1073/pnas.1016934108.

Boulard, E., Guyot, F., and Fiquet, G. (2012). The influence on Fe content on Raman spectra and unit cell parameters of magnesite-siderite solid solutions. *Phys. Chem. Miner.* 39, 239–246. doi:10.1007/s00269-011-0479-3.

Boulard, E., Guyot, F., Menguy, N., Corgne, A., Auzende, A.-L., Perrillat, J.-P., and Fiquet, G. (2018). CO_2-induced destabilization of pyrite-structured FeO_2H_x in the lower mantle. *Natl. Sci. Rev.* 5, 870–877. doi:10.1093/nsr/nwy032.

Cerantola, V., Bykova, E., Kupenko, I., Merlini, M., Ismailova, L., McCammon, C., et al. (2017). Stability of iron-bearing carbonates in the deep Earth's interior. *Nat. Commun.* 8. doi:10.1038/ncomms15960.

Desmaele, E., Sator, N., Vuilleumier, R. and Guillot, B. (2019). Atomistic simulations of molten carbonates: Thermodynamic and transport properties of the Li_2CO_3-Na_2CO_3-K_2CO_3 system. *J. Chem. Phys.* 150, 094504.

Du, X., Wu, M., Tse, J. S., and Pan, Y. (2018). Structures and Transport Properties of CaCO3 Melts under Earth's Mantle Conditions *ACS Earth Space Chem* 2, 1–8. doi:10.1021/acsearthspacechem.7b00100.

Dziewonski, A. M. and Anderson, D. L. (1981). Preliminary reference Earth model. *Phys. Earth Planet. Int.* 25, 297–356.

Drewitt, J. W. E., Jahn, S., Sanloup, C., de Grouchy, C., Garbarino, G. and Hennet L. (2015). Development of chemical and topological structure in aluminosilicate liquids and glasses at high pressure. *J. Phys.: Cond. Matt.* 27, 105103.

Eggert, J. H., Weck, G., Loubeyre, P., and Mezouar, M. (2002). Quantitative structure factor and density measurements of high-pressure in diamond anvil cells by x-ray diffraction: Argon and water. *Phys. Rev. B* 65, 174105.

Fischer, R. A., Campbell, A. J., Chidester, B. A., Reaman, D. M., Thompson, E. C., Pigott, J. S., et al. (2018). Equations of state and phase boundary for stishovite and $CaCl_2$-type SiO_2. *Am. Mineral.* 103, 792–802.

Foley, S. F. (2008). Rejuvenation and erosion of the cratonic lithosphere. *Nature Geosci.* 1, 503–510. doi:10.1038/ngeo261.

Frost, D., Liebske, C., Langenhorst, F., McCammon, C., Tronnes, R., and Rubie, D. (2004). Experimental evidence for the existence of iron-rich metal in the Earth's lower mantle. *Nature* 428, 409–412. doi:10.1038/nature02413.

Ghosh, D. B., Bajgain, S. K., Mookherjee, M., and Karki, B. B. (2017). Carbon-bearing silicate melt at deep mantle conditions. *Sci. Rep.* 7. doi:10.1038/s41598-017-00918-x.

Hammersley, A. P., Svensson, S. O., Hanfland, M., Fitch, A. N., and Hausermann, D. (1996). Two-dimensional detector software: From real detector to idealised image or two-theta scan. *High Press. Res.* 14, 235–248.

Hosemann, R. and Bagchi, S. N. (1962). *Direct Analysis of Diffraction by Matter* (Amsterdam: North-Holland).

Huang, F., Wu, Z., Huang, S., and Wu, F. (2014). First-principles calculations of equilibrium silicon isotope fractionation among mantle minerals. *Geochim. Cosmochim. Acta* 140, 509–520. doi:10.1016/j.gca.2014.05.035.

Hudspeth, J., Sanloup, C., and Kono, Y. (2018). Properties of molten $CaCO_3$ at high pressure. *Geochem. Persp. Let.* 7, 27–31. doi:10.7185/geochemlet.1815.

Huotari, S., Sahle, C. J., Henriquet, C., Al-Zein, A., Martel, K., Simonelli, L., et al. (2017). A large-solid-angle X-ray Raman scattering spectrometer at ID20 of the European Synchrotron Radiation Facility. *J. Sync. Rad.* 24, 521–530.

Kaminsky, F. (2012). Mineralogy of the lower mantle: A review of 'super-deep' mineral inclusions in diamond. *Earth Sci. Rev.* 110, 127–147. doi:10.1016/j.earscirev.2011.10.005.

Kaminsky, F., Matzel, J., Jacobsen, B., Hutcheon, I., and Wirth, R. (2016). Isotopic fractionation of oxygen and carbon in decomposed lower-mantle inclusions in diamond. *Mineral. Petrol.* 110, 379–385. doi:10.1007/s00710-015-0401-7.

Kang, N., Schmidt, M. W., Poli, S., Franzolin, E., and Connolly, A. D. (2015). Melting of siderite to 20 GPa and thermodynamic properties of $FeCO_3$-melt. *Chem. Geol.* 400, 34–43.

Kono, Y. , Kenney-Benson C., Hummer, D., Ohfuji H. , Park, C., Shen, G. , Wang, Y., Kavner, A., and Manning, C. E. (2014). Ultralow viscosity of carbonate melts at high pressures. *Nat. Comm.* 5, 5091.

Litasov, K. D. and Shatskiy, A. (2018). *Carbon-Bearing Magmas in the Earth's Deep Interior* (Amsterdam, The Netherlands: Elsevier), chap. 2. 43–82.

Litasov, K. D., Shatskiy, A., Ohtani, E., and Yaxley, G. M. (2013). Solidus of alkaline carbonatite in the deep mantle. *Geology* 41, 79–82. doi:10.1130/G33488.1.

Li, Z., Li, J.., Lange, R., Liu, J., and Militzer, B. (2017). Determination of calcium carbonate and sodium carbonate melting curves up to Earth's transition zone pressures with implications for the deep carbon cycle. *Earth Planet. Sci. Lett.* 457 395–402.

Liu, J., Lin, J.-F., and Prakapenka, V. B. (2015). High-Pressure Orthorhombic Ferromagnesite as a Potential Deep-Mantle Carbon Carrier. *Sci. Rep.* 5. doi:10.1038/srep07640.

Lobanov, S. S., Goncharov, A. F., and Litasov, K. D. (2015). Optical properties of siderite ($FeCO_3$) across the spin transition: Crossover to iron-rich carbonates in the lower mantle. *Am. Mineral.* 100, 1059–1064. doi:10.2138/am-2015-5053.

Lobanov, S. S., Stevanovic, V., Gavryushkin, P. N., Litasov, K. D., Greenberg, E., Prakapenka, V. B., Oganov, A. R. and Goncharov, Al. F. (2017). Raman spectroscopy and x-ray diffraction of sp(3) $CaCO_3$ at lower mantle pressures. *Phys Rev B* 96, 104101. doi:10.1103/PhysRevB.96.104101.

Maeda, F., Ohtani, E., Kamada, S., Sakamaki, T., Hirao, N., and Ohishi, Y. (2017). Diamond formation in the deep lower mantle: a high-pressure reaction of $MgCO_3$ and SiO_2. *Sci. Rep.* 7. doi:10.1038/srep40602.

Mao, H. K., Xu, J., and Bell, P. M. (1986). Calibration of the ruby pressure gauge to 800 kbar under quasi-hydrostatic conditions. *J. Geophys. Res.* 91, 4673–4676.

C. Meade and R. J. Hemley and H. K. Mao (1992). High-pressure x-ray diffraction of SiO_2 glass. *Phys. Rev. Lett.* 69, 1387–1390. doi:10.2138/am-2017-6161.

Merlini, M., Cerantola, V., Gatta, G. D., Gemmi, M., Hanfland, M., Kupenko, I., et al. (2017). Dolomite-IV: Candidate structure for a carbonate in the Earth's lower mantle. *Am. Mineral.* 102, 1763–1766. doi:10.2138/am-2017-6161.

Nishihara, Y., Nakayama, K., Takahashi, E., Iguchi, T., and i. Funakoshi, K. (2005). P-V-T equation of state of stishovite to the mantle transition zone conditions. *Phys. Chem. Min.* 31, 660–670.

Oganov, A., Glass, C., and Ono, S. (2006). High-pressure phases of $CaCO_3$: Crystal structure prediction and experiment. *Earth Planet. Sci. Lett.* 241, 95–103. doi:10.1016/j.epsl.2005.10.014.

Oganov, A. R., Ono, S., Ma, Y., Glass, C. W., and Garcia, A. (2008). Novel high-pressure structures of $MgCO_3$, $CaCO_3$ and CO_2 and their role in Earth's lower mantle. *Earth Planet. Sci. Lett.* 273, 38–47.

Petitgirard, S., Malfait, W. J., Sinmyo, R., Kupenko, I., Hennet, L., Harries, D., et al. (2015). Fate of $MgSiO_3$ melts at core-mantle boundary conditions. *P. Natl. Acad. Sci. USA* 112, 14186–14190. doi:10.1073/pnas.1512386112.

Sahle, C. J., Mirone, A., Niskanen, J., Inkinen, J., Krisch, M., and Huotari, S. (2015). Planning, performing and analyzing X-ray Raman scattering experiments. *J. Sync. Rad.* 22, 400–409.

Sanloup, C. (2016). Density of magmas at depth. *Chem. Geol.* 429, 51–59. doi:10.1016/j.chemgeo.2016.03.002.

Sanloup, C. and de Grouchy, C. J. L. (2018). *X-ray diffraction structure measurements* (Amsterdam, The Netherlands: Elsevier), chap. 5. 137–154.

Sanloup, C., Drewitt, J. W. E., Konôpková, Z., Dalladay-Simpson, P., Morton, D. M., Rai, N., et al. (2013). Structural change in molten basalt at deep mantle conditions. *Nature* 503, 104–107.

Sato, T. and Funamori, N. (2008). Sixfold-coordinated amorphous polymorph of SiO_2 under high pressure. *Phys. Rev. Lett.* 101, 255502.

Seto, Y., Hamane, D., Nagai, T., and Fujino, K. (2008). Fate of carbonates within oceanic plates subducted to the lower mantle, and a possible mechanism of diamond formation. *Phys. Chem. Miner.* 35, 223–229. doi:10.1007/s00269-008-0215-9.

Sharma, S. and Simons, B. (1979). *Raman study of K_2CO_3-$MgCO_3$ glasses* (Carnegie Institute), vol. 79. 322–326.

Shieh, S. R., Jarrige, I., Wu, M., Hiraoka, N., Tse, J. S., Mi, Z., et al. (2013). Electronic structure of carbon dioxide under pressure and insights into the molecular-to-nonmolecular transition. *Proc. Natl. Acad. Sci. U. S. A.* 110, 18402–18406. doi:10.1073/pnas.1305116110.

Smith, E. M., Shirey, S. B., Nestola, F., Bullock, E. S., Wang, J., Richardson, S. H., et al. (2016). Large gem diamonds from metallic liquid in earth's deep mantle. *Science* 354, 1403–1405.

Solomatova, N. V. and Asimow, P. D. (2018). First-principles calculations of high-pressure iron-bearing monoclinic dolomite and single-cation carbonates with internally consistent Hubbard U. *Phys. Chem. Miner.* 45, 293–302. doi:10.1007/s00269-017-0918-x.

Solomatova, N. V., Caracas, R., and Manning, C. E. (2019). Carbon sequestration during core formation implied by complex carbon polymerization. *Nat. Comm.* 10, 789. doi:10.1038/s41467-019-08742-9.

Stagno, V., Stopponi, V., Kono, Y., Manning, C. E. and Tetsuo, I. (2018). Experimental determination of the viscosity of Na_2CO_3 melt between 1.7 and 4.6 GPa at 1200-1700 degrees C: Implications for the rheology of carbonatite magmas in the Earth's upper mantle. *Chem. Geol.* 501,19–25. doi:10.1016/j.chemgeo.2018.09.036.

Vuilleumier, R., Seitsonen, A., Sator, N., and Guillot, B. (2014). Structure, equation of state and transport properties of molten calcium carbonate ($CaCO_3$) by atomistic simulations. *Geochim. Cosmchim. Acta* 141, 547–566. doi:10.1016/j.gca.2014.06.037.

Weis, C., Sternemann, C., Cerantola, V., Sahle, C. J., Spiekermann, G., Harder, M., et al. (2017). Pressure driven spin transition in siderite and magnesiosiderite single crystals. *Sci. Rep.* 7. doi:10.1038/s41598-017-16733-3.

Wilding, M. C., Wilson, M., Alderman, O. L. G., Benmore, C., Weber, J. K. R., Parise, J. B., et al. (2016). Low-dimensional network formation in molten sodium carbonate. *Sci. Reports* 6, 24415.

Yarger, J. L., Smith, K. H., Nieman, R. A., Diefenbacher, J., Wolf, G. H., Poe, B. T., McMillan, P. F. (1995). Al Coordination Changes in High-Pressure Aluminosilicate Liquids. *Science* 270, 1964–1967.

Zhang, Z., and Liu, Z. (2015). High pressure equation of state for molten $CaCO_3$ from first principles simulations. *Chin. J. Geochem.* 34, 13–20.

FIGURE CAPTIONS

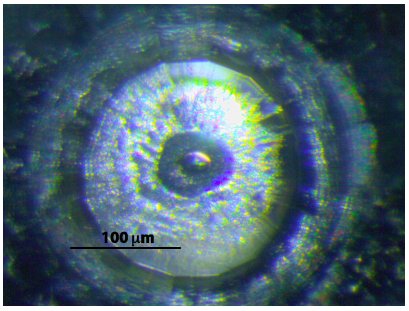

Figure 1. Microphotograph of the sample after laser heating at 110 GPa. Single shot laser heating resulted in the formation of a quasi-spherical pure carbonate glass that was removed from the gasket for EPMA and/or SEM analyses.

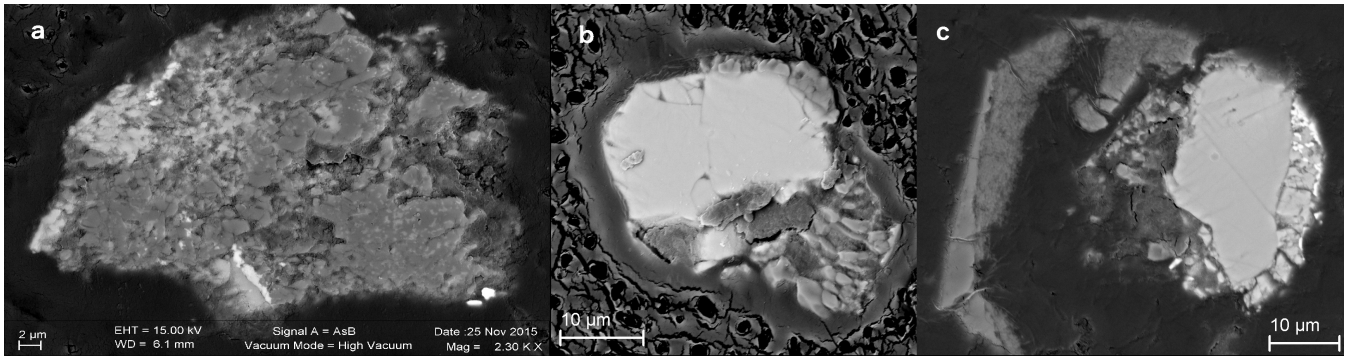

Figure 2. SEM images of recovered samples. Low P sample 8 (**a**) shows pervasive contamination of carbonate sample with SiO_2 P-transmitting medium. High P samples 9 (**b**) and 15 (**c**) show that chemical integrity of carbonate melt (homogeneous light gray zone) was preserved.

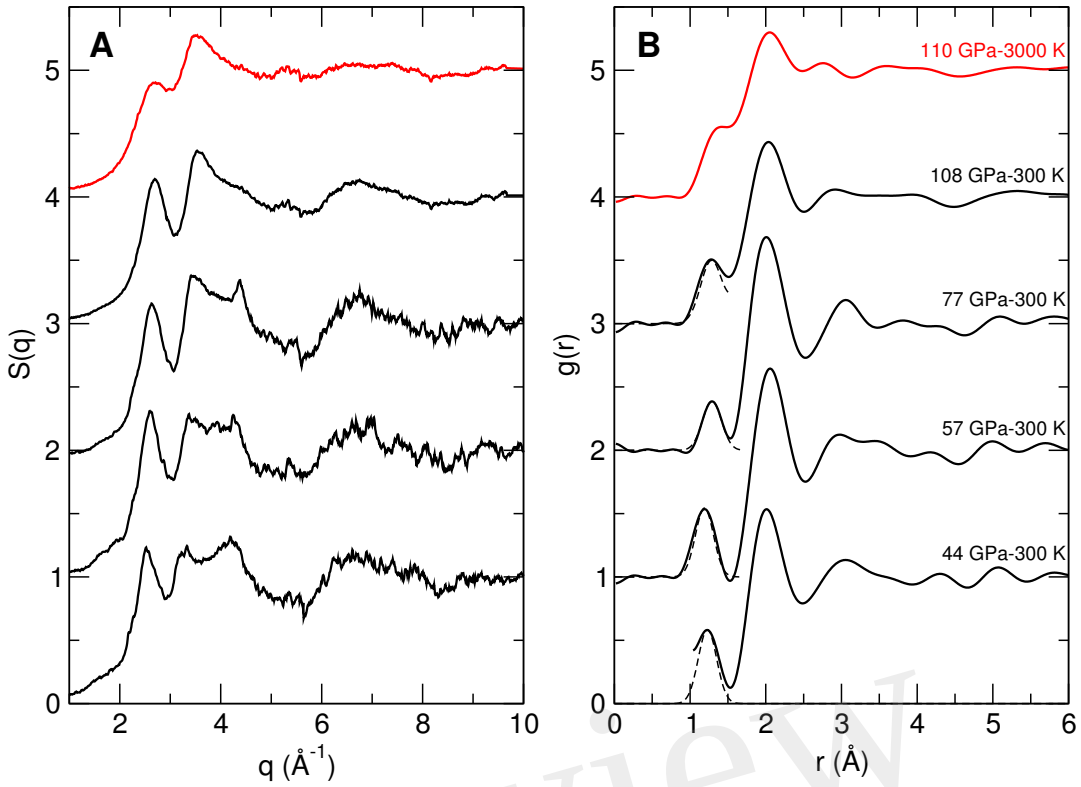

Figure 3. Structure of non-crystalline $FeCO_3$ at high pressures. **(A)** Structure factor, $S(q)$, for all quenched glasses (black) and the highest P melt (red). **(B)** Corresponding radial distribution functions, $g(r)$. Dashed lines are fits to the C-O contribution at 1.2-1.3 Å where there is no overlap with farther contributions.

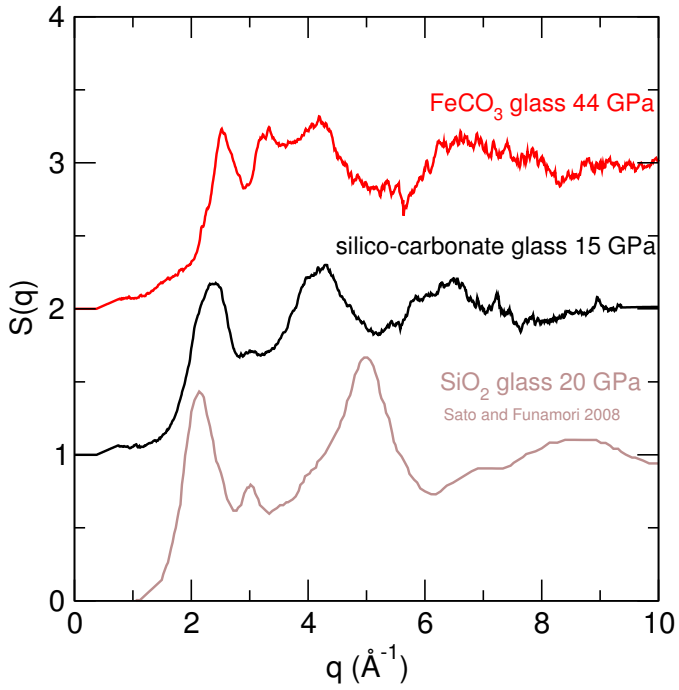

Figure 4. Structure factor, $S(q)$, for low P reacted $FeCO_3$+SiO_2 glass (black), compared to SiO_2 glass at 20 GPa (Sato and Funamori, 2008) (brown) and $FeCO_3$ glass at 44 GPa (red). Low P sample 8 (15 GPa) shows intermediate structure between SiO_2 glass and high P $FeCO_3$ glasses.

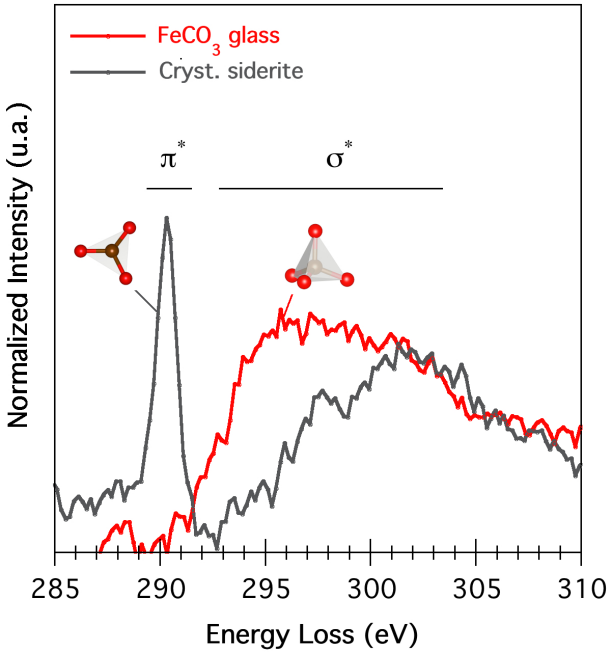

Figure 5. X-ray Raman spectra collected at the carbon K-edge on crystalline siderite and high P-quenched $FeCO_3$ glasses at ambient conditions. The disappearance of the π^* feature, which is solely related to the three-fold coordinated carbon, is a spectroscopic evidence of a full four-fold coordination state in the glassy structure of $FeCO_3$.

Table 1. Run conditions, quenched products and their chemical composition in wt% obtained from EMPA. One standard deviations are given in parentheses. Starting natural siderite sample also contained less than 0.1 wt% CaO and MnO.

#	P melt/glass (GPa)	CO_2	FeO	MgO	SiO_2	Total
6	11.6/ –	not recovered, reaction confirmed by XRD (Fig.4)				
8	15/14	25.7(9.2)	42.2(5.8)	0.1(0.1)	24.2(6.7)	92.2
15	51/44	40.6(0.5)	58.9(9.3)	0.3(0.1)	0.3(0.2)	100.0
13	55/–	41.2(2.6)	54.4(1.3)	0.3(0.2)	2.0(1.9)	98.0
20	63/57	36.6(6.8)	57.7(1.3)	0.4(0.4)	0.7(0.8)	95.4
9	79/72	not analyzed, C-coated for SEM (Fig.2)				
12	83/77	not recovered				
14	110/108	37.8(8.7)	58.5(1.1)	0.2(0.1)	0.7(0.8)	97.3
sample for x-ray Raman	59	not analyzed, only glass sphere preserved				

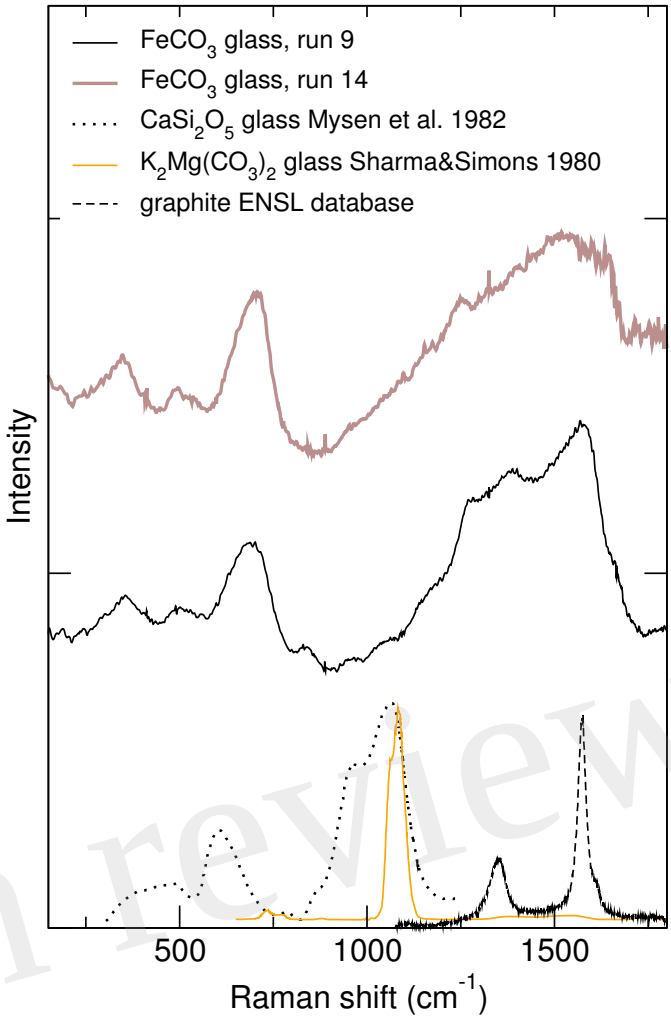

Figure 6. Raman spectra collected on high P-quenched $FeCO_3$ glasses (runs 9 and 14) at ambient conditions.

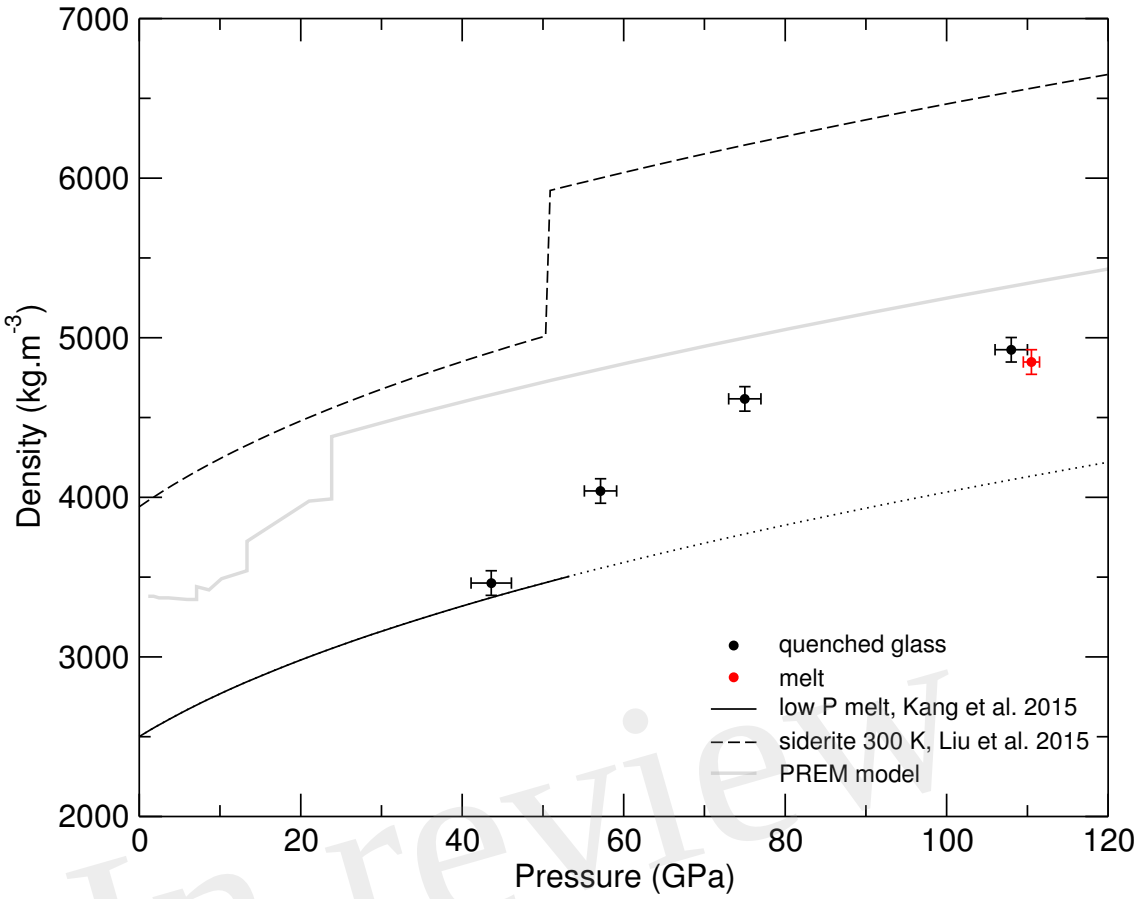

Figure 7. Density evolution of glassy, molten and cristalline siderite with pressure. Molten low P siderite (plain curve), high P data on glass (black points) and the highest P melt (red point), crystalline equation of state (dashed curve) includes the transition from high spin siderite I to low spin siderite II at 50 GPa (Liu et al., 2015).